LIGHT POLARIZATION

Polarization recovery through scattering media

Hilton B. de Aguiar,[1,2]* Sylvain Gigan,[3] Sophie Brasselet[1]*

The control and use of light polarization in optical sciences and engineering are widespread. Despite remarkable developments in polarization-resolved imaging for life sciences, their transposition to strongly scattering media is currently not possible, because of the inherent depolarization effects arising from multiple scattering. We show an unprecedented phenomenon that opens new possibilities for polarization-resolved microscopy in strongly scattering media: polarization recovery via broadband wavefront shaping. We demonstrate focusing and recovery of the original injected polarization state without using any polarizing optics at the detection. To enable molecular-level structural imaging, an arbitrary rotation of the input polarization does not degrade the quality of the focus. We further exploit the robustness of polarization recovery for structural imaging of biological tissues through scattering media. We retrieve molecular-level organization information of collagen fibers by polarization-resolved second harmonic generation, a topic of wide interest for diagnosis in biomedical optics. Ultimately, the observation of this new phenomenon paves the way for extending current polarization-based methods to strongly scattering environments.

INTRODUCTION

Accessing the structural organization of molecular assemblies is an important aspect of biological imaging. This organization determines important functions, such as the formation of biofilaments, and also contributes to clinical disorders, such as in the growth of amyloids in neurodegenerative diseases. Polarization-resolved microscopy is able to provide molecular structural insights beyond the diffraction-limited scale (*1*), and, being noninvasive and nondestructive, could in principle be used for deep in vivo structural imaging.

Unfortunately, light propagation through multiple scattering media, such as thick biological tissues, inherently scrambles polarization states. After injection of a well-defined polarization state and wave vector directions, each successive scattering event rotates both wave vector and polarization directions (*2*, *3*). Thus, multiple scattering ultimately leads to a "depolarized" speckle (schematically sketched in Fig. 1A). This random scrambling makes molecular structural imaging impossible to be performed deep in biological media. It is highly detrimental for polarization-resolved studies because no predetermined relation with the incoming polarization state exists anymore: This is indeed a prerequisite for the analysis of the polarized response and its relation to structural modeling (*1*).

Wavefront shaping has revolutionized imaging deep in scattering media (*4*) by recreating a focus that can be used for microscopy with subcellular resolution. By coherently controlling the speckle pattern generated from multiple scattering events, one can increase the energy density at targeted positions locally building a constructive interference. Wavefront shaping allows spatial and temporal (*5*–*7*) refocusing of light through (*8*, *9*), or inside (*10*–*12*), scattering media as a result of the manipulation of the wavefront phase or amplitude (*13*, *14*).

Despite remarkable achievements for refocusing purposes, wavefront shaping techniques are not compatible yet with polarization-resolved microscopy. When light propagates through a scattering medium, the expected outcome is no more a simple far-field free-space relation with the incident polarized wavefront. Nevertheless, the obtained speckle is related to the input field. The electric field at position m in the output speckle is related to the input field at position n through the scalar transmission matrix $\mathbf{t}$ ($E_m = \sum_n t_{mn} E_n$) (*15*). Although this formalism has been introduced for monochromatic light, it is still valid for broadband light, and we shall consider it in what follows (*16*). The measurement of the transmission matrix has allowed to refocus light through a scattering medium, leading to considerable linear (*15*) and nonlinear (*17*) intensity enhancements, even when performed under broadband conditions (*17*). In this scalar formalism, one assumes that a well-defined polarization state at the input will lead to a deterministic polarization state at the output if, for instance, one places a polarizer at the detection. Depolarization arises from the lack of correlations among the t^{ij}_{mn} elements of the vectorial transmission matrix (*18*), which relates the input field E^j_n with the polarization state j to the output field E^i_m with the polarization state i. Thus, to refocus with output polarization state control, one needs to perform polarization-sensitive measurements of the vectorial transmission matrix (*18*–*20*); that is, polarizing optical elements are necessary to "force" a defined polarization state, a task not permissible upon an eventual refocusing inside scattering media. The determinism of the output polarization state is of uttermost importance for polarization-resolved approaches, because an emitted signal that is polarization-modulated (for example, a nonlinear process) requires a well-controlled linear excitation polarization state.

Here, we demonstrate an effect that enables polarization-resolved imaging through scattering media using a single transmission matrix measurement. We show in particular that the measurement of the transmission matrix under broadband conditions leads to polarization recovery (Fig. 1B), an effect that forms the basis for prospective deep molecular structural imaging. After acquiring a broadband transmission matrix of the system, one can use its information to shape the wavefront and refocus at desired positions. We show that, despite the presence of a depolarized speckle before wavefront shaping, one can retrieve a pure polarization state at the refocus. Remarkably, the refocus polarization state is robust upon a change at the input state, thus showing that polarization-resolved microscopy is possible under multiple scattering conditions.

RESULTS

Depolarization from an unshaped wavefront

We first discuss aspects related to the speckle without wavefront shaping. We performed experiments at controlled optical thickness

[1]Aix Marseille Univ, CNRS, Centrale Marseille, Institut Fresnel, F-13013 Marseille, France. [2]Département de Physique, Ecole Normale Supérieure/PSL Research University, CNRS, 24 rue Lhomond, 75005 Paris, France. [3]Laboratoire Kastler Brossel, ENS-PSL Research University, CNRS, UPMC Sorbonne Universitées, Collège de France, 24 rue Lhomond, 75005 Paris, France.
*Corresponding author. Email: h.aguiar@phys.ens.fr (H.B.d.A.); sophie.brasselet@fresnel.fr (S.B.)

(L/l_t) using phantoms with scattering properties similar to biological media (see Materials and Methods). To aid the discussion, the inset of Fig. 2A shows simplified schematics of the polarization state combinations used. Figure 2A (red dashed line) shows the spatially averaged degree of linear polarization (DOLP) of the speckle observed outside the medium [DOLP = $(I_{\parallel} - I_{\perp})/(I_{\parallel} + I_{\perp})$, where I is intensity and $\parallel$ and $\perp$ are two orthogonal directions of the input polarization with respect to the fixed analyzed polarization]. As L/l_t increases, the averaged speckle polarization state decreases its correlation with the initial linearly polarized one, as evidenced by the decrease in the spatially averaged DOLP. Such a situation precludes any polarization-resolved approach given that the a priori known relation between the input and output polarization states is lost because of multiple scattering phenomena.

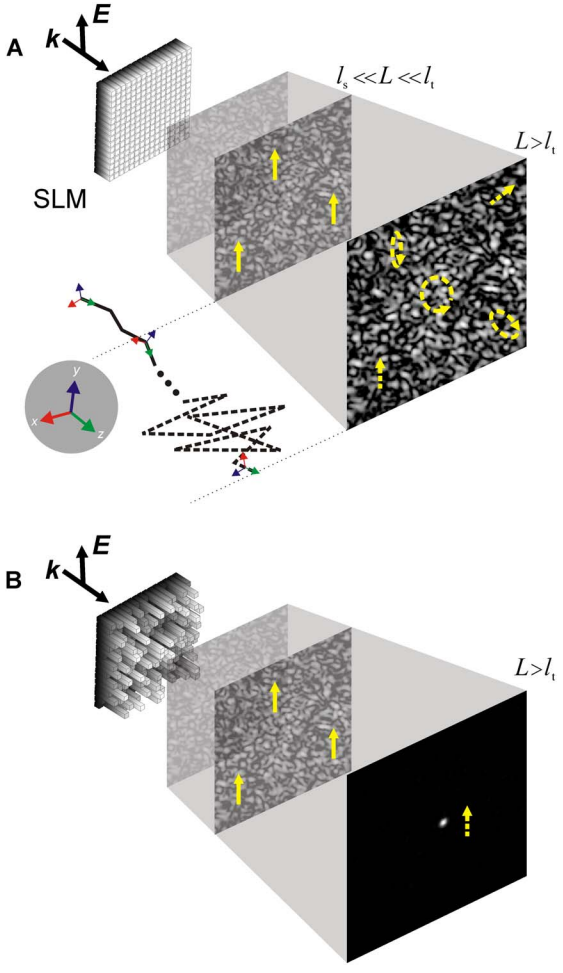

Fig. 1. Illustration of polarization state scrambling during propagation in a scattering medium and principle of polarization recovery via wavefront shaping. When light propagates in a scattering medium, the wavefront is rapidly deformed into a speckle pattern (at depths comparable to the scattering mean free path l_s), but polarization scrambling occurs on a different length scale. In the forward scattering regime (as typically found in biological tissues), when the thickness L is smaller than the transport mean free path l_t, forward scattering events mainly conserves the initial polarization state. (**A**) In the diffusive regime $L > l_t$ for an unshaped wavefront, the polarization of the speckle gradually scrambles and lacks any resemblance with the input one. The bottom panel illustrates how, during propagation, each forward scattering conserves polarization (continuous line) and how polarization is mixed when entering the diffusive regime (dashed line). (**B**) In contrast, we observe that an optimal wavefront shaped by a spatial light modulator (SLM) not only is able to refocus light but also recovers the original polarization state even without any polarizing optics in the detection, under broadband source illumination.

Polarization recovery from broadband wavefront shaping

In contrast, when performing wavefront shaping, the outcome becomes very different. To find the optimal wavefronts, a broadband transmission matrix is first acquired (*17*) without any selection of output polarization state (see Materials and Methods for details on the experimental layout). In practice, this is equivalent to acquiring experimental transmission matrix elements $t_{mn}^{(exp)} = t_{mn}^{xx} + t_{mn}^{yx}$. Once the transmission matrix is known, we can selectively refocus light at targeted positions (Fig. 2A, upper right panel) (*15*). Surprisingly, upon rotation of the input polarization state, the refocus does not degrade. A very different result should be expected from previous work on polarized wavefront shaping

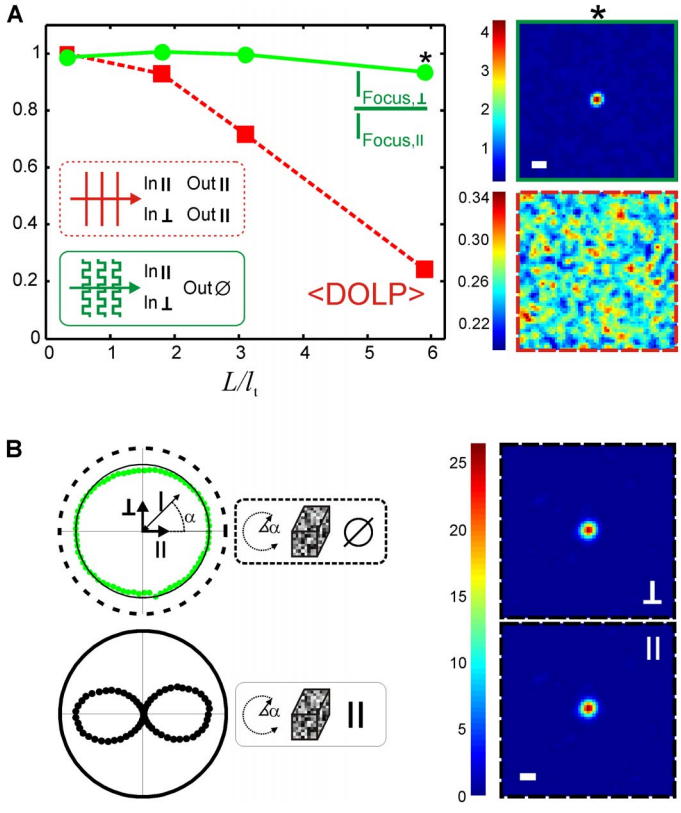

Fig. 2. Experimental quantification of polarization recovery. (**A**) Left: Averaged DOLP of the speckle (<DOLP>) (red squares) and refocus intensity ratio after wavefront shaping ($I_{\parallel}/I_{\perp}$; corresponding to the same wavefront but rotated input polarization) (green circles), as a function of optical depths L/l_t. Polarization scrambling of the speckle occurs for lengths of the order of l_t. Nevertheless, at depths of several l_t, after shaping, the refocus intensity survives a change of 90° of the input polarization. Right: Speckle image after (top) and before (bottom) the wavefront shaping procedure. The scattering media are made of 5-μm-diameter polystyrene beads. The asterisk symbol (*) in the box refers to the images shown on the right. (**B**) Similar experiments performed using 1-mm-thick opaque acute brain slice coronal cross section as a scattering medium. Top left: Nonanalyzed refocus intensity (green circles) upon rotation of the excitation field. Right: Images show the refocus at two input polarization states ($\perp$ and $\parallel$) with the same intensity scale. Bottom left: The refocus polarization state purity is evaluated by placing an analyzer and observing an extinction (black circles). Scale bars, 1 μm.

(*18*, *19*), which showed that each incident polarization state is related to a particular transmission matrix of the medium. This should lead to a rapid loss of the refocus efficiency upon incident polarization rotation. The significant difference from these previous findings is the broadband regime used, which differs considerably from a monochromatic regime. We further quantified this resilience to a change in input state as intensity ratio between the two injected polarization states ($I_{\parallel}/I_{\perp}$), as shown in Fig. 2A (continuous line). The quantity $I_{\parallel}/I_{\perp}$ is of ultimate importance for polarization-resolved microscopy, because one typically evaluates a change in output readout upon change in input polarization state. Clearly, only minute degradation of the refocus intensity ratio is seen even when reaching depths in the diffusive regime (L/l_t), in marked contrast with the DOLP measurements. A similar effect was observed through a 1-mm-thick opaque brain slice, where the dependence of the refocus intensity with respect to the incident polarization is almost constant, as shown in a polar plot representation in Fig. 2B (top left panel) (fig. S1 presents similar plots in a linear scale).

We quantified the quality of the polarization state obtained at the refocus. Remarkably, the optimally shaped wavefront refocuses light with a well-defined polarization state, although no output polarization state is privileged. First, we observed no depolarized or elliptical contribution in the refocus, as evidenced by the complete extinction of its intensity upon placement of an analyzer (Fig. 2B, bottom left panel). Second, a complete characterization of the polarization state at the refocus, using polarimetry, shows that the purity of the obtained polarization is very high, with a degree of polarization above 94% independently of the input (linear) polarization state (see fig. S2). In contrast, the low-intensity background speckle remaining around the refocus exhibits strong depolarization signatures (see fig. S2).

The results above indirectly reveal correlations of the polarization-related part of the vectorial transmission matrix elements because they imply $t^{xx}_{mn} \approx t^{yy}_{mn}$. These correlations are formally shown in Fig. 3A as cross-correlation of a set of measurements where t^{xx}_{mn} and t^{yy}_{mn} are independently measured for the same realization of disorder (with the polarization state combination shown in Fig. 3A). In this analysis, whose procedure is explained in the Supplementary Materials (see fig. S3), the peak above the noise confirms that the diagonal submatrices $\mathbf{t}^{ii}$ of the vectorial transmission matrix are highly correlated. In contrast, the off-diagonal submatrices $\mathbf{t}^{ij}$ exhibit poor correlation with the diagonal ones and low amplitudes (see fig. S4). For comparison with a situation closer to those of previous studies (*18*–*20*), when acquiring the monochromatic transmission matrix, the diagonal matrices $\mathbf{t}^{ii}$ do not exhibit strong correlation properties (see fig. S5) (*21*, *22*), evidencing that polarization recovery is not likely to occur under monochromatic conditions at large optical thicknesses.

The monochromatic and broadband responses differ in several aspects. In the monochromatic case, the polarized speckle contrast is high regardless of the combination of polarizations used (Fig. 3B, left panel). As the number of scattering events, or equivalently the optical thickness, increases, the polarization state of the speckle becomes scrambled, given the development of an orthogonal polarization state with comparable properties. Because the speckle contrast is related to the amplitude of the acquired transmission matrix, all elements of the submatrices $\mathbf{t}^{ii}$ and $\mathbf{t}^{ij}$ participate equally to the refocus intensity, leading to unpredictable polarization states (*19*, *20*). Furthermore, these two orthogonal states lead to decorrelated speckles for large optical thicknesses, explaining the poor correlation observed in the transmission matrix elements (fig. S5) (*21*).

The behavior under broadband conditions is very different. First, the speckle contrast is lower than in the monochromatic case (Fig. 3B, right panel). This is the result of the incoherent superposition of uncorrelated individual speckle spectral modes (*4*). Second, the speckle contrasts measured along parallel and perpendicular polarization outputs, with respect to a fixed input polarization, differ considerably (Fig. 3B, right panel). The consequence is a lower contribution of this orthogonal component to the acquired broadband transmission matrix, making polarization recovery possible. An explanation of this lower contribution can be found in the time of flight of photons leaving the medium. We observe that the time of flight of photons in averaged speckle grains is much longer than the input pulse length. Upon wavefront shaping, we observe a considerable intensity decrease of the long path length photons in the time-of-flight measurements (see fig. S6). Therefore, the process of measuring the transmission matrix under broadband conditions is responsible for the selection of short path lengths in the refocus, which is consistent with the recovery of the incident polarization state given that long path lengths are more likely to undergo depolarization. However, these short path lengths should not be confused with ballistic light. The refocus properties exhibit all characteristics of a nonballistic process, with reduced spot size and large intensity enhancements (see fig. S7). Finally, as photons that undergo

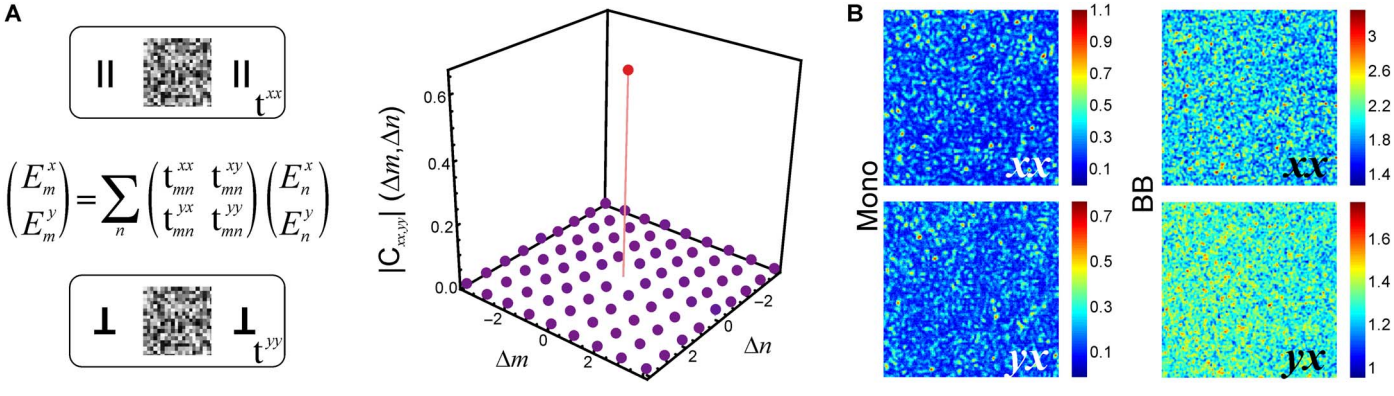

Fig. 3. Experimental quantification of vectorial transmission matrix correlations and the origin of the polarization recovery. (**A**) Cross-correlation of vectorial transmission matrix elements with polarization combinations *xx* and *yy* for $L/l_t \approx 6$. The peak confirms strong correlation between the matrix elements, thus explaining the resilience of the refocus to a polarization state change. (**B**) Images of the output speckle parallel (*xx*) and perpendicular (*yx*) to the input polarization state for a monochromatic (Mono) source (left panel) and a broadband (BB) source (right panel) for $L/l_t \approx 6$.

a low number of scattering events retain a high level of spectral and polarization coherence, they presumably lead to a polarization-memory effect (*3*). The reason for these coherence preservation properties might be related to the interference process performed under broadband conditions when measuring the transmission matrix. The interferometric measurement is likely to induce path length–dependent weighting, leaving all long path length photons under destructive interferences that contribute to a small, depolarized speckle background.

Polarized nonlinear imaging through scattering media

We used the polarization recovery to demonstrate nonlinear structural imaging through scattering media. Figure 4 shows the experimental layout and representative results of a wavefront shaping experiment. In the first step, a polarization combination is used where the analyzer and incoming polarization state are aligned together, that is, a configuration measuring the t^{xx}_{mn} elements. Note that the presence of the analyzer is not necessary for a wavefront shaping experiment, but it supports an unambiguous proof of structural imaging (see below). After acquiring the broadband transmission matrix, we spatially refocus light in a raster scanning fashion and acquire in parallel the enhanced second harmonic generation (SHG) signal from nanocrystals of potassium titanyl phosphate (nanoKTP). The dipolar character of nanoKTP ensures that no ambiguity exists in the polarization state evaluation. The refocused light generates efficient SHG from the nanoscopic sources, as seen by the two nanoparticles in Fig. 4B (left panel). In the second step, a second imaging scan using the very same optimal wavefronts is taken (Fig. 4B, right panel), however, with the incoming polarization state rotated 90°. The refocus after the scattering medium still persists and highlights the second particle, revealing the orientation-dependent nonlinear efficiency. This emphasizes the presence of nanoKTP crystals with different orientations, which are identified using the same wavefront. Any oriented nonlinear source could be probed in the same way, highlighting its molecular order organization in a scattering medium.

Biomolecular structural imaging through scattering media

These observations have implications in the field of structural nonlinear imaging in biology. In particular, collagen I present in the extracellular matrix of tissues is known to be an important biomedical marker for the progression of tumors using SHG (*23*). Its polarization-resolved SHG signals have been shown to report crucial information on the loss of integrity of collagen fibrils in the progression of the pathology (*24*). However, it is not possible to perform these experiments deep in biological tissues because of multiple scattering. In Fig. 5A, without wavefront shaping, the polarization-resolved SHG signals are unable to report molecular-level organization of collagen, as shown by the speckle-like SHG image (Fig. 5A, left panel) and its almost isotropic response to an incoming rotating polarization (Fig. 5A, right panel).

We showcase high-resolution SHG imaging of collagen fibers and the retrieval of their molecular-level state (Fig. 5B). To mimic a nonlinear microscopy experiment, we placed the collagen fiber after the scattering medium with a characterized transmission matrix. Unlike the previous experiment, here we exploit the memory effect to raster-scan the refocus (*25*, *26*): A tilt of the wavefront leads to a displacement

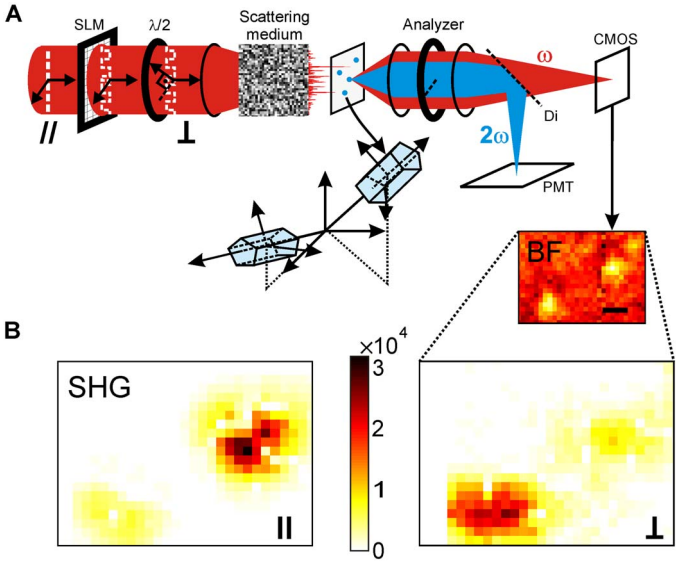

Fig. 4. Demonstration of structural imaging through scattering media–exploiting transmission matrix correlations. (**A**) Simplified experimental layout used in the experiments. Ultrashort pulse wavefronts are shaped by an SLM and focused on the scattering medium. The speckle transmitted by the scattering medium excites the nonlinear sources (nanoKTP) placed at a plane further imaged on a complementary metal-oxide semiconductor (CMOS) camera and a photomultiplier tube (PMT). (**B**) Demonstration of structural imaging by polarization-resolved SHG. In the first step, the vectorial transmission matrix elements t^{xx}_{mn} are acquired and used to raster-scan the refocus, thus generating the SHG images (left panel). The bottom-right inset in (A) shows the bright-field (BF) image at the same region of interest (ROI), where two particles can be seen. In the second step, only the excitation polarization is rotated, and a second scan is taken (5× rescaled) (right panel) using the very same t^{xx}_{mn} elements. Scale bar, 1 μm.

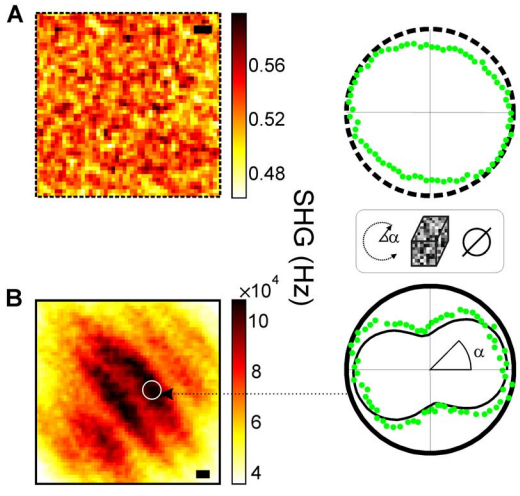

Fig. 5. Applications of transmission matrix correlations for biological specimen SHG structural imaging. (**A**) Raster-scanning rat tail collagen tendon placed after a thin diffuser, with an unshaped wavefront, leads to a featureless SHG image (left panel). Furthermore, the SHG intensity response upon turning the input polarization (right panel) is almost isotropic, an outcome that is not representative of the molecular structure of collagen. (**B**) Raster-scanning using the memory effect, from a known transmission matrix, generates morphological features reminiscent of collagen fibers (left panel). By refocusing on a specific fiber, we recorded the intensity response of the SHG signal upon turning the input polarization angle (right panel). The continuous line (black) is a fit to the data (green circles) from which we retrieve the fiber-scale nonlinear susceptibility values of collagen. The retrieved nonlinear susceptibilities reveal the molecular order of the fibers and are in agreement with previous observations. In the polar plots, the radial direction represents SHG intensity. Scale bar, 1 μm.

of the speckle behind the medium. This methodology is able to provide highly contrasted SHG images of rat tendon specimens where clear fibers can be seen running along the diagonal of the images (Fig. 5B, left panel). In this demonstration, we do not use an analyzer to detect the SHG: In an eventual refocusing inside a scattering medium, the nonlinearly generated photon polarization state would be scrambled. Therefore, molecular structural imaging is only insightful if performed in a nonanalyzed configuration (*27*). By fixing the refocus position in a fiber and rotating the excitation polarization state, we can still perform a polarization-resolved study (*28*, *29*). Figure 5B (right panel) shows the background-subtracted SHG intensity (green circles) and a fit (black continuous line) using a known model for molecular orientations in collagen (*1*, *24*, *30*). The retrieved nonlinear optical constants of collagen are in agreement with previously reported values (Supplementary Materials contain further information on the analysis of the SHG) (*30*).

DISCUSSION AND CONCLUSIONS

According to our model, a laser source with a bandwidth larger than the medium bandwidth (*16*, *17*, *31*), with a differential output polarization contrast, leads to the recovery of the original polarization state. We corroborate this model by performing further measurements with a picosecond laser source that exhibits a bandwidth closer to the medium bandwidth, but still smaller than it. We confirm the capacity of polarization recovery under this regime, supported by the observation of a differential output polarization contrast (see section S7). Nevertheless, an exact determination of the transition (from complete depolarization to recovery) demands a full characterization that is not accessible by our current lasers. To address this transition, one needs a tunable bandwidth source that reaches tens to hundreds of picometer bandwidth for biological media at the optical thickness treated here.

To date, there are no microscopic models that take into consideration the broadband vectorial nature of light propagation in a scattering medium in a fully deterministic way. Although we have phenomenologically pinpointed the microscopic origin of the new effect, there still remains the question of the memory of the polarization state. Although current understanding of polarization state scrambling in the monochromatic regime is established (*21*, *22*) by statistical methods, however, microscopic modeling such a bulk complex anisotropic scattering system under broadband conditions is currently challenging (see an extensive discussion in section S8) (*32*–*34*). First, there is a lack of theoretical methods to describe light propagation using finite coherence lengths, a key point necessary for broadband sources with a larger bandwidth than the bandwidth of the medium. Second, it is only more recently that wavefront shaping experiments have started to be tackled theoretically, highlighting another challenge in modeling. Although there has been some progress for describing averaged quantities, such as field-field correlations (*32*, *33*), a deterministic non-averaged approach is necessary to model the wavefront shaping experiment. Despite that there has been progress in this direction, the current tools are mostly limited to two-dimensional systems (*35*–*38*) and focused on the monochromatic regime of small systems using approximations that can be questioned in the case of biological media (such as often assuming $l_t = l_s$). Therefore, we hope that the outcome presented here will trigger new developments in theoretical models to unravel the microscopic explanation of the robustness of the polarization recovery and memory observed upon using broadband sources.

In conclusion, we have shown how to retrieve the original input polarization state after multiple scattering events without using any polarizing optics at the detection. This was possible because of a broadband acquisition of the transmission matrix of the scattering system together with wavefront shaping. We further demonstrated how this phenomenon enabled molecular-level microscopy by a polarization-resolved approach at unprecedented depths in biological specimens. Although we demonstrate the implications for nonlinear structural imaging through the scattering medium, there have been recent efforts on refocusing inside the scattering medium (*39*), which can directly exploit the outcomes found here in the optically thin regime. As a prospective work, we expect the reported correlations to have profound consequences in other various approaches that can reach the diffusive regime ($L/l_t > 1$). For example, acoustic-based methods (*11*, *12*, *40*) are known to be able to refocus light in the diffuse regime with cellular resolution. This means that the acoustic signal from the obtained refocus could perform structural analysis: If light absorbers are organized in an ordered way, a rotation of the refocus optical polarization, using the very same wavefront, should lead to a change in the acoustic signal.

MATERIALS AND METHODS

Optical setup

The optical layout used for all experiments is presented in Fig. 4A. Ultrashort pulses (800-nm central wavelength, 8-nm bandwidth for femtosecond regime, and 0.37-nm bandwidth for picosecond regime) (repetition rate, 76 MHz; Mira, Coherent) were steered onto a 256 × 256–pixel reflective SLM (Boulder Nonlinear Systems). The SLM was imaged on the back focal plane of the focusing lens (achromatic lens, f = 19 mm; AC127-019-B-ML, Thorlabs), with the scattering medium placed after it. The nanoKTP crystals were imaged by an objective (40×; numerical aperture, 0.75; Nikon) on a 12-bit CMOS camera (Flea3, Point Grey) and on a large-area photon-counting PMT (MP 953, PerkinElmer). The SHG signal was spectrally separated with a suitable 560-nm long-pass dichroic mirror (AHF Analysentechnik) and 700-nm short-pass (FESH0700, Thorlabs) and 400 ± 20–nm band-pass (Chroma Technology) filters. Additionally, a 650-nm long-pass filter (FELH0650, Thorlabs), a linear polarizer, and a zero-order half-wave plate (46-555, Edmund Optics)—placed in a motorized rotation stage—were used for the excitation beam before the focusing lens. An analyzer (WP25M-UB, Thorlabs) was used to select the detected polarization state whenever stated in the main text.

Broadband transmission matrix measurement, wavefront shaping, and nonlinear imaging methodology

A thorough description of the methods used for acquisition of the transmission matrix can be found elsewhere (*12*, *15*). It consists of a two-step process: First, the broadband transmission matrix of the system is acquired and then used for selective refocusing in an ROI. Briefly, for each input-output channel, phase and amplitude of the corresponding transmission matrix element were obtained by phase-shifting interferometry. The wavefront phase of a Hadamard base (input channel) was shifted with respect to a reference field in the range of 0 to 2π, with its intensity recorded by a CMOS pixel (output channel). A Fourier transform was applied on the output channel interferogram of the nth Hadamard basis, thus retrieving its phase and amplitude. Once all the Hadamard bases were measured, a unitary transformation was applied to obtain the transmission matrix in the canonical basis (*33*). The only difference in this study from the studies of Chaigne *et al.* (*12*) and Popoff *et al.* (*15*) is that the method used here was applied using an ultrashort broadband source, whose bandwidth is larger than the medium

spectral bandwidth at large thicknesses [see definition in the studies of Andreoli *et al.* (*16*), de Aguiar *et al.* (*17*), and Paudel *et al.* (*41*)]. To acquire the nonlinear images, we used two methodologies. In Fig. 4, we raster-scanned the refocus at each spatial position in the ROI containing the nanoKTP and, in parallel, collecting the SHG signal integrated within the imaged plane with the large-area PMT. In Fig. 5, we raster-scanned the refocus using the memory effect: A linear phase ramp was added to the wavefront, thus displacing the refocus in the image plane (with the SHG signal acquired in parallel). The numbers of controlled SLM segments for the experiments were 2^{12} (Fig. 4) and 2^{10} (Figs. 2, 3, and 5).

Sample preparation

Various types of scattering media were used: dispersions of 5-μm-diameter polystyrene beads (Figs. 2A and 3), 1-mm-thick brain slice (Fig. 2B) (both fixed in agarose solution), 1-mm-thick paraffin film (Fig. 4) (*42*), and a commercial diffuser (10° Light Shaping Diffuser, Newport; Fig. 5). The rat tendon (Fig. 5) was placed between two coverslips separated by a 120-μm-thick spacer and filled with agarose solution. We followed the same protocol for the 1-mm-thick mouse brain coronal cross section (Fig. 2B), except that the spacer was 1 mm thick. The nanoKTP crystals (150 nm in diameter) were previously characterized by various methods (*43*) and were drop-cast on a coverslip (170 μm thick). The scattering mean free path, l_s, of the scattering media in Figs. 2A and 3 (l_s = 53 to 69 μm) was determined by measuring the extinction of the laser through a thin dispersion slab of known thickness, with scattered light and ballistic light spatially isolated in the Fourier space (*27*). The anisotropy value g for calculating $l_t = l_s/(1 - g)$ was obtained using the scattering pattern from Mie theory.

SUPPLEMENTARY MATERIALS

Supplementary material for this article is available at http://advances.sciencemag.org/cgi/content/full/3/9/e1600743/DC1

section S1. Polarization state evaluation
section S2. Vectorial transmission matrix analysis under broadband conditions
section S3. Comparison with a monochromatic transmission matrix
section S4. Time-of-flight results
section S5. Exclusion of ballistic hypothesis
section S6. Model for nonanalyzed SHG response
section S7. On the role of bandwidth
section S8. Discussion on theoretical models
fig. S1. Polarization state evaluation of the refocused light for the brain specimen.
fig. S2. Polarization state evaluation of the refocused light.
fig. S3. Effect of transmission matrix interelement coupling on cross-correlation.
fig. S4. Cross-correlation between various transmission matrices.
fig. S5. Comparison of different transmission matrix acquisition methods.
fig. S6. Time-of-flight results.
fig. S7. Size of the refocus, enhancement, contrast, and ballistic contribution versus optical thickness.
fig. S8. Bandwidth results.
References (*44*–*56*)

REFERENCES AND NOTES

1. S. Brasselet, Polarization-resolved nonlinear microscopy: Application to structural molecular and biological imaging. *Adv. Opt. Photonics* **3**, 205–271 (2011).
2. D. Bicout, C. Brosseau, A. S. Martinez, J. M. Schmitt, Depolarization of multiply scattered waves by spherical diffusers: Influence of the size parameter. *Phys. Rev. E* **49**, 1767–1770 (1994).
3. M. Xu, R. R. Alfano, Random walk of polarized light in turbid media. *Phys. Rev. Lett.* **95**, 213901 (2005).
4. A. P. Mosk, A. Lagendijk, G. Lerosey, M. Fink, Controlling waves in space and time for imaging and focusing in complex media. *Nat. Photonics* **6**, 283–292 (2012).
5. O. Katz, E. Small, Y. Bromberg, Y. Silberberg, Focusing and compression of ultrashort pulses through scattering media. *Nat. Photonics* **5**, 372–377 (2011).
6. D. J. McCabe, A. Tajalli, D. R. Austin, P. Bondareff, I. A. Walmsley, S. Gigan, B. Chatel, Spatio-temporal focusing of an ultrafast pulse through a multiply scattering medium. *Nat. Commun.* **2**, 447 (2011).
7. J. Aulbach, B. Gjonaj, P. M. Johnson, A. P. Mosk, A. Lagendijk, Control of light transmission through opaque scattering media in space and time. *Phys. Rev. Lett.* **106**, 103901 (2011).
8. Z. Yaqoob, D. Psaltis, M. S. Feld, C. Yang, Optical phase conjugation for turbidity suppression in biological samples. *Nat. Photonics* **2**, 110–115 (2008).
9. I. M. Vellekoop, A. P. Mosk, Focusing coherent light through opaque strongly scattering media. *Opt. Lett.* **32**, 2309–2311 (2007).
10. R. Horstmeyer, H. Ruan, C. Yang, Guidestar-assisted wavefront-shaping methods for focusing light into biological tissue. *Nat. Photonics* **9**, 563–571 (2015).
11. B. Judkewitz, Y. M. Wang, R. Horstmeyer, A. Mathy, C. Yang, Speckle-scale focusing in the diffusive regime with time reversal of variance-encoded light (TROVE). *Nat. Photonics* **7**, 300–305 (2013).
12. T. Chaigne, O. Katz, A. C. Boccara, M. Fink, E. Bossy, S. Gigan, Controlling light in scattering media non-invasively using the photoacoustic transmission matrix. *Nat. Photonics* **8**, 58–64 (2013).
13. D. Akbulut, T. J. Huisman, E. G. van Putten, W. L. Vos, A. P. Mosk, Focusing light through random photonic media by binary amplitude modulation. *Opt. Express* **19**, 4017–4029 (2011).
14. D. B. Conkey, A. M. Caravaca-Aguirre, R. Piestun, High-speed scattering medium characterization with application to focusing light through turbid media. *Opt. Express* **20**, 1733–1740 (2012).
15. S. M. Popoff, G. Lerosey, R. Carminati, M. Fink, A. C. Boccara, S. Gigan, Measuring the transmission matrix in optics: An approach to the study and control of light propagation in disordered media. *Phys. Rev. Lett.* **104**, 100601 (2010).
16. D. Andreoli, G. Volpe, S. Popoff, O. Katz, S. Grésillon, S. Gigan, Deterministic control of broadband light through a multiply scattering medium via the multispectral transmission matrix. *Sci. Rep.* **5**, 10347 (2015).
17. H. B. de Aguiar, S. Gigan, S. Brasselet, Enhanced nonlinear imaging through scattering media using transmission-matrix-based wave-front shaping. *Phys. Rev. A* **94**, 043830 (2016).
18. S. Tripathi, R. Paxman, T. Bifano, K. C. Toussaint, Vector transmission matrix for the polarization behavior of light propagation in highly scattering media. *Opt. Express* **20**, 16067–16076 (2012).
19. Y. Guan, O. Katz, E. Small, J. Zhou, Y. Silberberg, Polarization control of multiply scattered light through random media by wavefront shaping. *Opt. Lett.* **37**, 4663–4665 (2012).
20. J.-H. Park, C. Park, H. Yu, Y.-H. Cho, Y. Park, Dynamic active wave plate using random nanoparticles. *Opt. Express* **20**, 17010–17016 (2012).
21. I. Freund, M. Kaveh, B. Berkovits, M. Rosenbluh, Universal polarization correlations and microstatistics of optical waves in random media. *Phys. Rev. E* **42**, 2613–2616 (1990).
22. S. M. Cohen, D. Eliyahu, I. Freund, M. Kaveh, Vector statistics of multiply scattered waves in random systems. *Phys. Rev. A* **43**, 5748–5751 (1991).
23. R. M. Williams, W. R. Zipfel, W. W. Webb, Interpreting second-harmonic generation images of collagen I fibrils. *Biophys. J.* **88**, 1377–1386 (2005).
24. R. Ambekar, T.-Y. Lau, M. Walsh, R. Bhargava, K. C. Toussaint, Quantifying collagen structure in breast biopsies using second-harmonic generation imaging. *Biomed. Opt. Express* **3**, 2021–2035 (2012).
25. S. Schott, J. Bertolotti, J.-F. Léger, L. Bourdieu, S. Gigan, Characterization of the angular memory effect of scattered light in biological tissues. *Opt. Express* **23**, 13505–13516 (2015).
26. B. Judkewitz, R. Horstmeyer, I. M. Vellekoop, I. N. Papadopoulos, C. Yang, Translation correlations in anisotropically scattering media. *Nat. Phys.* **11**, 684–689 (2015).
27. H. B. de Aguiar, P. Gasecka, S. Brasselet, Quantitative analysis of light scattering in polarization-resolved nonlinear microscopy. *Opt. Express* **23**, 8960–8973 (2015).
28. J. Duboisset, D. Aït-Belkacem, M. Roche, H. Rigneault, S. Brasselet, Generic model of the molecular orientational distribution probed by polarization-resolved second-harmonic generation. *Phys. Rev. A* **85**, 043829 (2012).
29. F.-Z. Bioud, P. Gasecka, P. Ferrand, H. Rigneault, J. Duboisset, S. Brasselet, Structure of molecular packing probed by polarization-resolved nonlinear four-wave mixing and coherent anti-Stokes Raman-scattering microscopy. *Phys. Rev. A* **89**, 013836 (2014).
30. P. Stoller, K. M. Reiser, P. M. Celliers, A. M. Rubenchik, Polarization-modulated second harmonic generation in collagen. *Biophys. J.* **82**, 3330–3342 (2002).
31. N. Curry, P. Bondareff, M. Leclercq, N. F. van Hulst, R. Sapienza, S. Gigan, S. Grésillon, Direct determination of diffusion properties of random media from speckle contrast. *Opt. Lett.* **36**, 3332–3334 (2011).
32. K. Vynck, R. Pierrat, R. Carminati, Multiple scattering of polarized light in disordered media exhibiting short-range structural correlations. *Phys. Rev. A* **94**, 033851 (2016).
33. K. Vynck, R. Pierrat, R. Carminati, Polarization and spatial coherence of electromagnetic waves in uncorrelated disordered media. *Phys. Rev. A* **89**, 013832 (2014).

34. G. Osnabrugge, S. Leedumrongwatthanakun, I. M. Vellekoop, A convergent Born series for solving the inhomogeneous Helmholtz equation in arbitrarily large media. *J. Comput. Phys.* **322**, 113–124 (2016).
35. W. Choi, A. P. Mosk, Q.-H. Park, W. Choi, Transmission eigenchannels in a disordered medium. *Phys. Rev. B* **83**, 134207 (2011).
36. M. Davy, Z. Shi, J. Park, C. Tian, A. Z. Genack, Universal structure of transmission eigenchannels inside opaque media. *Nat. Commun.* **6**, 6893 (2015).
37. C. W. Hsu, A. Goetschy, Y. Bromberg, A. D. Stone, H. Cao, Broadband coherent enhancement of transmission and absorption in disordered media. *Phys. Rev. Lett.* **115**, 223901 (2015).
38. O. S. Ojambati, H. Yılmaz, A. Lagendijk, A. P. Mosk, W. L. Vos, Coupling of energy into the fundamental diffusion mode of a complex nanophotonic medium. *New J. Phys.* **18**, 043032 (2016).
39. I. N. Papadopoulos, J.-S. Jouhanneau, J. F. A. Poulet, B. Judkewitz, Scattering compensation by focus scanning holographic aberration probing (F-SHARP). *Nat. Photonics* **11**, 116—123 (2017).
40. Y. M. Wang, B. Judkewitz, C. A. DiMarzio, C. Yang, Deep-tissue focal fluorescence imaging with digitally time-reversed ultrasound-encoded light. *Nat. Commun.* **3**, 928 (2012).
41. H. P. Paudel, C. Stockbridge, J. Mertz, T. Bifano, Focusing polychromatic light through strongly scattering media. *Opt. Express* **21**, 17299–17308 (2013).
42. C.-L. Hsieh, Y. Pu, R. Grange, G. Laporte, D. Psaltis, Imaging through turbid layers by scanning the phase conjugated second harmonic radiation from a nanoparticle. *Opt. Express* **18**, 20723–20731 (2010).
43. L. Mayer, A. Slablab, G. Dantelle, V. Jacques, A.-M. Lepagnol-Bestel, S. Perruchas, P. Spinicelli, A. Thomas, D. Chauvat, M. Simonneau, T. Gacoin, J.-F. Roch. Single KTP nanocrystals as second-harmonic generation biolabels in cortical neurons. *Nanoscale* **5**, 8466–8471 (2013).
44. S. M. Popoff, G. Lerosey, M. Fink, A. C. Boccara, S. Gigan, Controlling light through optical disordered media: Transmission matrix approach. *New J. Phys.* **13**, 123021 (2011).
45. D. Goldstein, *Polarized Light* (Marcel Dekker, 2003).
46. A. Aubry, A. Derode, Random matrix theory applied to acoustic backscattering and imaging in complex media. *Phys. Rev. Lett.* **102**, 084301 (2009).
47. M. Mounaix, D. Andreoli, H. Defienne, G. Volpe, O. Katz, S. Grésillon, S. Gigan, Spatiotemporal coherent control of light through a multiple scattering medium with the multispectral transmission matrix. *Phys. Rev. Lett.* **116**, 253901 (2016).
48. I. M. Vellekoop, A. Lagendijk, A. P. Mosk, Exploiting disorder for perfect focusing. *Nat. Photonics* **4**, 320–322 (2010).
49. D. Di Battista, G. Zacharakis, M. Leonetti, Enhanced adaptive focusing through semi-transparent media. *Sci. Rep.* **5**, 17406 (2015).
50. S. Roth, I. Freund, Second harmonic generation in collagen. *J. Chem. Phys.* **70**, 1637–1643 (1979).
51. I. Amat-Roldan, S. Psilodimitrakopoulos, P. Loza-Alvarez, D. Artigas, Fast image analysis in polarization SHG microscopy. *Opt. Express* **18**, 17209–17219 (2010).
52. D. Aït-Belkacem, A. Gasecka, F. Munhoz, S. Brustlein, S. Brasselet, Influence of birefringence on polarization resolved nonlinear microscopy and collagen SHG structural imaging. *Opt. Express* **18**, 14859–14870 (2010).
53. E. E. Gorodnichev, A. I. Kuzovlev, D. B. Rogozkin, Depolarization coefficients of light in multiply scattering media. *Phys. Rev. E* **90**, 043205 (2014).
54. L. F. Rojas-Ochoa, D. Lacoste, R. Lenke, P. Schurtenberger, F. Scheffold, Depolarization of backscattered linearly polarized light. *J. Opt. Soc. Am. A* **21**, 1799–1804 (2004).
55. D. A. Zimnyakov, J.-T. Oh, Y. P. Sinichkin, V. A. Trifonov, E. V. Gurianov, Polarization-sensitive speckle spectroscopy of scattering media beyond the diffusion limit. *J. Opt. Soc. Am. A* **21**, 59–70 (2004).
56. R. Sarma, A. G. Yamilov, S. Petrenko, Y. Bromberg, H. Cao, Control of energy density inside a disordered medium by coupling to open or closed channels. *Phys. Rev. Lett.* **117**, 086803 (2016).

Acknowledgments: We are grateful to M. Mounaix for valuable support on the time-of-flight measurement and discussions in its interpretation. We also thank E. Andressen and H. Rigneault for fruitful discussions and support, A. Malvache and R. Cossart for providing the brain slices, T. Gacoin and L. Meyer for providing the nanoKTP particles, and K. Vynck for fundamental input on the theoretical challenges. **Funding:** This work was supported by the FEMTO Network and contracts ANR-10-INBS-04-01 (France BioImaging infrastructure network), ANR-11-INSB-0006 (France Life Imaging infrastructure network), and ANR-15-CE19-0018-01 (MyDeepCARS). H.B.d.A. was supported by LabEX ENS-ICFP (Ecole Normale Supérieure–International Centre for Fundamental Physics) (ANR-10-LABX-0010/ANR-10-IDEX-0001-02 PSL). S.G. was funded by the European Research Council (grant 278025-COMEDIA). **Author contributions:** H.B.d.A. and S.B. conceived and developed the ideas with fundamental input from S.G. H.B.d.A. developed and performed all experiments and processed and analyzed the data. All authors contributed to the writing and editing of the manuscript. **Competing interests:** The authors declare that they have no competing interests. **Data and materials availability:** All data needed to evaluate the conclusions in the paper are present in the paper and/or the Supplementary Materials. Additional data related to this paper may be requested from the authors. Requests for materials should be addressed to H.B.d.A. and S.B.

Submitted 7 April 2016
Accepted 5 August 2017
Published 1 September 2017
10.1126/sciadv.1600743

Citation: H. B. de Aguiar, S. Gigan, S. Brasselet, Polarization recovery through scattering media. *Sci. Adv.* **3**, e1600743 (2017).

Polarization recovery through scattering media

Hilton B. de Aguiar, Sylvain Gigan and Sophie Brasselet

Sci Adv **3** (9), e1600743.
DOI: 10.1126/sciadv.1600743